New estimates of the pan-Arctic sea ice–atmosphere neutral drag coefficients from ICESat-2 elevation data

Alexander Mchedlishvili[1], Christof Lüpkes[2], Alek Petty[3,4], Michel Tsamados[5], and Gunnar Spreen[1]

[1]Institute of Environmental Physics, University of Bremen, Bremen, Germany
[2]Alfred Wegener Institute for Polar and Marine Research, Bremerhaven, Germany
[3]Goddard Space Flight Center, National Aeronautics and Space Administration, Greenbelt, MD, USA
[4]University of Maryland, College Park, MD, USA
[5]Department of Earth Sciences, University College London, London, UK

Correspondence: Alexander Mchedlishvili (alexander.mchedlishvili@uni-bremen.de)

Abstract. The effect that sea ice topography has on the momentum transfer between ice and atmosphere is not fully quantified due to the vast extent of the Arctic and limitations of current measurement techniques. Here we present a method to estimate pan-Arctic momentum transfer via a parameterization which links sea ice–atmosphere form drag coefficients with surface feature height and spacing. We measure these sea ice surface feature parameters using the Cloud and land Elevation

5 Satellite-2 (ICESat-2) which, though it cannot resolve as well airborne surveys, has a higher along-track spatial resolution than other contemporary altimeter satellites. As some narrow obstacles are effectively smoothed out by the ICESat-2 ATL07 spatial resolution, we use near-coincident high-resolution Airborne Topographic Mapper (ATM) elevation data from NASA's Operation IceBridge (OIB) mission to scale up the regional ICESat-2 drag estimates. By also incorporating drag due to open water, floe edges and sea ice skin drag, we produced a time series of average total pan-Arctic neutral atmospheric drag coefficient

10 estimates from October 2018 to May 2022. Here we have observed its temporal evolution to be unique and not directly tied to sea ice extent. By also mapping 3-month aggregates for the years 2019, 2020 and 2021 for better regional analysis, we found the thick multiyear ice area directly north of the Canadian Archipelago and Greenland to be consistently above $2.0 \cdot 10^{-3}$ with rough ice $\sim 1.5 \cdot 10^{-3}$ typically filling the full multiyear ice portion of the Arctic each spring.

1 Introduction

15 Arctic sea ice is heterogeneous with respect to several characteristics including its concentration, thickness, and roughness (e.g., Thorndike et al., 1975; Bourke and Garrett, 1987). The understanding of how these parameters vary with space and time is important for several reasons, including its impact on human activities, e.g. navigation, and its impact on the physical system, e.g. the transfer of momentum and energy between the atmosphere and ocean.

Studies of Arctic sea ice have arguably focused more on constraining variability in concentration and thickness, towards

20 estimating sea ice volume and its variability in time and space. However, the surface roughness of sea ice also exhibits strong spatial and temporal variability (e.g., Andreas et al., 2010; Lüpkes et al., 2012; Castellani et al., 2014; Petty et al., 2017) which needs to be better understood. Sea ice roughness is driven in-part by pressure ridging, which redistributes ice vertically, as well

as the presence of snow features such as dunes and sastrugis (e.g., Arya, 1975; Hopkins, 1998; Petty et al., 2016). Summer melt can facilitate the smoothing of obstacles like ridges but can also increase roughness through ice melt (e.g., Andreas et al.,

25   2010; Landy et al., 2015; Castellani et al., 2014). Rougher sea ice is generally found in the thick, multiyear ice regions north of the Arctic Archipelago and Greenland. Newly formed first-year ice is typically much smoother, although this division is complicated by the accumulation of snow and its ability to smooth out ice surface variability (e.g., Garbrecht et al., 2002). Observational (e.g., Castellani et al., 2014) and model studies (e.g., Tsamados et al., 2014) suggest that sea ice roughness varies more with space, e.g. between first-year ice and multiyear ice regions, than it does with time, e.g. between freeze-up and

30   melt seasons. With the decline of multiyear ice due to recent sea ice minima (e.g., Stroeve et al., 2012), the Central Arctic as well as areas north of Eurasia and Alaska are predominantly composed of first-year ice during winter months and are therefore smoother in comparison (e.g., Castellani et al., 2014; Petty et al., 2017).

The roughness of sea ice is heavily linked with its motion as a result of momentum and energy transfer between ocean, sea ice and atmosphere. Disregarding the proportionally little Arctic sea ice that is fastened to the surrounding landmasses, the

35   remaining majority is subject to motion from the balance of drag forces from ocean currents and winds as well as internal forces (e.g., Thorndike and Colony, 1982; Steele et al., 1997). Ice motion redistributes ice and snow around the Arctic and controls the rate of discharge from the Arctic basin. The balance of forces governing this motion is described in the momentum balance equation for sea ice, in which the interactions between ice, atmosphere and ocean are quantified via drag coefficients. The turbulent surface flux of momentum $\boldsymbol{\tau}$ that describes this interaction is as follows

40    $$\boldsymbol{\tau} = \rho C_d(z) U(z) \left(\cos\theta \, \boldsymbol{U}(z) + \sin\theta \, \hat{k} \times \boldsymbol{U}(z) \right) \tag{1}$$

where z represents height above sea level and is most commonly set to a reference height of 10 m to match the layer for which the Monin Obukhov theory for the determination of turbulent fluxes is valid. It is furthermore nearest to the lowest height level of high-resolution climate and weather prediction models. ρ is the air density, $\boldsymbol{U}(z)$ is the difference in air and ice velocities at a given height z and $U(z)$ is its magnitude, $\hat{k}$ is the vertical unit vector and θ is the turning angle. The drag coefficient C_d

45   is usually written as a product of C_d^n and f_m. f_m is a stability and surface roughness dependent function (e.g., Birnbaum and Lüpkes, 2002; Lüpkes and Gryanik, 2015; Gryanik and Lüpkes, 2018). C_d^n is a neutral drag coefficient that assumes a neutrally stratified atmospheric surface layer, and is the key parameter that is investigated in this study. The total drag coefficient over a given sea ice surface is commonly subdivided into a contribution from skin drag $C_{d,s}$, caused by microscale roughness, and a contribution by form drag $C_{d,f}$, caused by large distinct obstacles (Arya, 1973, 1975). This division is the basis for the drag

50   parameterization developed by Garbrecht et al. (2002). The derived parameterization is developed for estimating the form drag component of the total neutral 10 meter drag coefficient $C_{d10,f}^n$ from the distribution of distinct obstacles and their heights relative to the surface.

Since the difference in air and ice velocities $\boldsymbol{U}(z)$ varies with space and time, so too does the the associated momentum transfer and, by extension, drag forces. Given the changing Arctic climate, and the above-mentioned shift from multiyear ice to

55   first-year ice, we can expect that, with a changing distribution of spatial roughness, the associated drag forces will change also. It is therefore in our best interest to help constrain drag coefficients to better model sea ice–atmosphere momentum transfer

and in turn, the Arctic climate system. In this study, we will be focusing on the interaction between the atmosphere and sea ice and the related atmospheric (wind) drag force, and will avoid extrapolating our findings to the equally important interaction between ocean and sea ice since our observations are limited to satellite and airborne measurements.

60   The Garbrecht et al. (2002) parameterization, discussed further in subsequent sections, has been used successfully in various Arctic regions using airborne topographic data (Castellani et al., 2014; Petty et al., 2017). We now aim to extend the applicability of said parameterization onto the high-resolution pan-Arctic topographic data measured by the Advanced Topographic Laser Altimeter System (ATLAS) onboard NASA's Ice, Cloud and land Elevation Satellite-2 (ICESat-2) and better characterize the spatio-temporal variability in form drag. With this data product we hope to aid the development of future climate models

65   with integrated form drag parameterization schemes (e.g., Tremblay and Mysak, 1977; Steiner et al., 1999; Tsamados et al., 2014; Yu et al., 2020; Elvidge et al., 2021). Model studies with integrated form drag schemes have been shown to better characterize both ice–atmosphere and ice-ocean interactions as well as inherent properties of sea ice like its thickness (e.g., Tsamados et al., 2016; Martin et al., 2016). However, the degree of uncertainty remains large primarily due to a lack of constraints in these form drag parameterization schemes. While airborne topographic data is perhaps the best record of measured sea ice drag

70   coefficients in the Arctic, it cannot reliably be used to constrain model drag coefficients because of its incomplete temporal and spatial coverage. Satellite drag coefficient evaluations using topography data, on the other hand, have in the past been impractical due to their inability to detect sea ice roughness on sufficiently small scales (e.g., Landy et al., 2015; Castellani et al., 2014). With the launch of NASA's ICESat-2 laser altimeter satellite in 2018, which is able to collect topographic data over sea ice at a resolution that is higher than its predecessors (10s of meters - able to resolve distinct sea ice features), this

75   study aims to make use of the advancements in satellite altimetry to estimate the neutral drag coefficients across the entire Arctic and highlight its regional and seasonal variability for the first time.

2   Data and Methods

This section describes the data-sets involved in this study as well as the parameterizations used to calculate drag coefficients.

2.1   ATLAS on ICESat-2

80   The Advanced Topographic Laser Altimeter System (ATLAS) is a lidar instrument onboard ICESat-2 that collects high resolution surface elevation data using a sophisticated split-beam photon counting laser system (Neumann et al., 2019). By determining the travel time of reflected laser pulses, ATLAS is able to accurately measure small changes in topography through differences in along-track elevation. The six laser beams are divided into three beam pairs consisting of a strong and a weak beam. The separation between each of the beam pairs is about 3.3 km across-track, whereas the separation between the strong

85   and weak beams making up the pairs is 2.3 km along-track and 90 m across-track. At an altitude of 500 km, the 10 kHz laser pulses that ATLAS transmits result in roughly 11 m diameter laser footprints (Magruder et al., 2020, 2021) that are spaced 0.7 m apart. Here what we refer to as a footprint is the spatial extent of the laser energy illumination on the observed surface (Magruder et al., 2020).

In this study we focus on the along-track heights for sea ice and open water leads (ICESat-2 ATL07/L3A level 3a data product). ATL07/L3A takes the global geolocated photon data (ATL03/L2) as input and further processes it to obtain information on sea ice topography (e.g., Kwok et al., 2021a, 2019b). For each of the six laser beams, estimates of sea ice surface heights are computed by applying various filters (to remove background photons) and a dual-Gaussian fit to segments of varying length, over which 150 signal photons are accumulated. This is done to reduce the vertical errors from ∼30 cm for each photon height to ∼2 cm (over flat surfaces) for each ATL07 segment height (Kwok et al., 2019a). The segment length varies based on surface type which influences photon counts such that when photon counts are low, segment length is high and vice versa (Kwok et al., 2021a). The spatial resolution is then the sum of the segment length and beam footprint and are on average ∼ 30 m for the strong beams and ∼ 70 m for the weak beams (Kwok et al., 2019a). The strong beams (beams 1, 3 and 5) are roughly 4 times stronger in terms of pulse energy than the weak beams (beams 2, 4 and 6), which results in these segment length differences (Kwok et al., 2019b). As a result, we only use the three strong beams for this study to take advantage of the better resolution that they provide. The retrieved heights are referenced to the WGS84 ellipsoid and include various geophysical corrections (e.g. ocean tides, inverted barometer, mean sea surface). ATLAS distinguishes water and ice surfaces by utilizing the surface photon rate, the width of the photon distribution and background rate (Kwok et al., 2021a). ATL07 is also restricted to regions of ice concentration greater than 15% based on passive microwave data.

2.2 ATM Lidar on Operation IceBridge airplanes

The Airborne Topograhic Mapper (ATM) is an instrument suite that contains two high-resolution conically scanning laser altimeters at 1.5° and 2.5° off-nadir, able to measure surface elevation with swath widths 245 m and 40 m, respectively (Studinger, M. 2013, updated 2020; MacGregor et al., 2021; Studinger et al., 2022). Like ATLAS, the lidar uses a 532 nm laser (narrow scanner also uses 1064 nm laser) and a 10 kHz pulse repetition frequency with each laser spot having a footprint of ∼1 m and a vertical precision of ∼10 cm (Martin et al., 2012; Studinger et al., 2022). Here we use the wide scanner (1.5° off-nadir) to take advantage of its high data density at the edges of the swath. NASA carried out several airborne campaign in the Arctic and Antarctic named "Operation IceBridge" (OIB) during recent years targeting land and sea ice observations (MacGregor et al., 2021). Throughout OIB the ATM lidar instrument has been installed aboard and carried by NASA aircrafts (NASA P3-B and NASA DC8 aircrafts) (Kwok et al., 2019a).

The OIB ATM data-set used in this study is from April 2019 when 4 of the flights over sea ice are near-coincident in space and time with ICESat-2. This includes all data from 8, 12, 19 and 22 April 2019 throughout which coincidence was variable but sufficient for comparing observations of similar ice regimes (Kwok et al., 2019a). This data-set is used to derive a scaling factor via regression with ICESat-2 ATL07-derived drag coefficients as it is has a better spatial resolution and therefore better resolves sea ice features. By applying this factor to the ICESat-2 ATL07-derived drag coefficients using near-coincident OIB ATM data, we hope to mitigate the spatial sampling biases discussed in section 3. In addition, the 6 and 20 April 2019 flights across sea ice that were not coincident with any ICESat-2 tracks, are used to independantly evaluate our ICESat-2 ATL07 monthly pan-Arctic neutral drag coefficient estimates. The OIB flight lines are outlined in Fig. 3A of section 3.

2.3 Extracting sea ice feature data

The Garbrecht et al. (2002) sea ice drag parameterization requires obstacle (sea ice feature e.g., a pressure ridge, rubble field, hummock, snow dune, sastrugi) height and spacing for the calculation of drag coefficients. Regional averages of these quantities are derived from the ATL07 data over segments that are chunked prior to the sea ice feature extraction. After experimenting with multiple segment sizes over which to calculate those regional averages, 10 km segments were chosen as in Castellani et al. (2014). 10 kilometres is a typical grid length of a high-resolution regional climate model and is proposed to be a reasonable minimum for the drag parameterizations used (Garbrecht et al., 2002; Lüpkes et al., 2012). Importantly, the data is not equally spaced due to the influence of surface reflectively on photon counts and thus the along-track distance parameter (in meters) is used to chunk the data into 10 km segments. As a result, the 10 km segments end up having a similar but not equal amount of values. To see the typical spacing between measurements Arctic-wide and the spatial variability thereof, see Fig. A1B in A. Lastly, to increase the number of segments and the stability of drag estimates, the 10 km segments over which average sea ice feature statistics are calculated are shifted by 1 km along-track, i.e., they have large overlap and only every 10th segment is fully uncorrelated. Importantly, 10 km segments with a measurement spacing that exceeds 1 km, a value that is sufficiently higher than what can be attributed to dark non-reflective surfaces, are assumed to have cloud contamination and are therefore omitted.

After segmentation, the surface level is subtracted from all values per 10 km segment. While the surface height estimates are referenced with respect to the mean sea surface (Kwok et al., 2021a), the drag calculations require obstacle heights above level ground and not the sea surface (freeboard). Thus the sea ice heights are first binned (rounded to the nearest centimeter) and then the height of the surface level is calculated by computing the mode for all heights within the 10 km segment. By subtracting this mode, all heights are referenced to the regional ice level surface. For bimodal distributions, the higher mode is used so as to avoid modes associated to leads and young ice.

The produced 10 km segments of elevation from the regional sea ice surface are used to calculate average obstacle height and obstacle spacing per segment. A four-step process is applied to each segment to compute these regional parameters.

1. The first step involves finding local maxima, i.e. obstacle heights along the segment.

2. The second step is to omit obstacle heights that are below a chosen threshold value.

3. The third step is to distinguish individual features by omitting obstacles that do not fulfil the Rayleigh Criterion (explained below).

4. Finally the fourth step is to compute the spacing between the obstacles that fulfil the Rayleigh Criterion.

After omitting all elevation maxima (obstacles) that do not fulfil the Rayleigh Criterion, the obstacle heights and the spacing between them (both in meters) are averaged over each 10 km segment, before calculating the neutral drag coefficients at this same scale.

While the chosen threshold value of 0.2 m elevation is expected to detect not only pressure ridges but also all topographic features like rubble fields and hummocks, here we define an obstacle as any series of connected elevation values above the

155   cutoff. This is because all obstacles have the ability to impart form drag and it is therefore not necessary to distinguish between them. Despite this, a more ridge-focused threshold value of 0.8 m was also tested and produced similar results (not shown).

    As will be shown in section 3, the higher resolution OIB ATM data, that is able to better resolve sea ice features, is used to bias correct and account for sampling differences in ICESat-2 ATL07 data. Prior to extracting sea ice features, the conically scanned along-track topographic two dimensional data from ATM must also be converted into a one dimensional track. To do

160   so, we adopt the methods from Petty et al. (2017) wherein using a given azimuth angle range we can isolate different parts of the conically scanned ATM swath. We use the ranges 355 to 5 ° and 175 to 185 ° to extract the outermost narrow parts of the full ATM swath with the highest data density. This narrow track is then ordered as a function of distance from the first data point and interpolated to fix the resolution at 1 m along-track. Once ordered, as with ICESat-2 ATL07 elevation data, the OIB ATM data set undergoes the 10-km chunking and the four-step process outlined above.

165   The OIB ATM high-resolution airborne data-set is then processed and drag coefficients are calculated from the sea ice feature statistics obtained for 10 km segments (see section 2.4 for more about the calculation step). The processed OIB ATM data serves as an independent drag coefficient estimate to which we compare the processed ICESat-2 ATL07 data. The comparison is done on a regional scale by binning both output datasets onto a polar stereographic projection grid with nominal gridded resolution of 25 km. The Polar Stereographic projections is true at 70 degrees north with up to 6% distortion at the poles (Knowles, 1993);

170   making it an ideal candidate for pan-Arctic maps. The resampling step for the two datasets is done to compare drag coefficients averaged over the same area; this is because the 10-km segments are not perfectly aligned with one another. Once all coincident grid-cells are identified the bivariate distribution of the two gridded data products is generated.

    We use the OIB ATM data as reference to account for the spatial sampling differences with the lower resolution ICESat-2 data. A Huber Regressor is calculated from filled grid cells of near-coincident data and model parameters are then used to

175   linearly scale up the ICESat-2 ATL07 drag coefficient estimates. Unlike the traditional linear fit, the Huber Regressor applies a linear loss to samples with an absolute error $|z|$ larger than a given threshold value ϵ (set to 1.35 to achieve 95% statistical efficiency), thereby weighting 'inliers' and 'outliers' differently (Huber and Ronchetti, 2009). This is done to reduce the sensitivity of the loss function to outliers that are expected in the data due to the high level of uncertainty when comparing quantities averaged over large spatial scales. Importantly, OIB ATM data is taken as the independent true variable upon training

180   the model as ICESat-2 ATL07 is expected to underestimate obstacles due its lower spatial resolution and therefore overestimate obstacle spacing because of the cutoff.

2.4   Calculating neutral form drag coefficient

With the extracted sea ice feature statistics, we apply to them the form drag parameterization developed in Garbrecht et al. (2002). The parameterization is based on the formulation of Garbrecht et al. (1999), which itself is built upon findings by Arya

185   (1973, 1975); Hanssen-Bauer and Gjessing (1988) on momentum fluxes by single obstacles. While there are other parameterizations of surface drag (e.g., Lüpkes et al., 2012, 2013; Tsamados et al., 2014), here we focus on the one by Garbrecht et al. (2002) as it is optimized for one-dimensional data like ICESat-2 ATL07 and better suited for estimating drag due to obstacles over consolidated ice-cover.

The generalized Garbrecht et al. (2002) formulation for the atmosphere-ice form drag coefficient is as follows

$$C_{d,z_r,f} = \frac{1}{2} \frac{c_w}{\Delta x} \left[\frac{1}{\ln(z_r/z_0) - \Psi(z_r/L)} \right]^2 \int_{z_0}^{H_r} [\ln(z/z_0) - \Psi(z/L)]^2 \, dz \qquad (2)$$

where c_w is the coefficient of resistance, z_r is the reference height, z_0 is surface roughness length and $\Psi(z/L)$ is the Monin Obukhov stability correction function. H_r and Δx represent obstacle height and obstacle spacing respectively which, as in Garbrecht et al. (2002), we will generalize to ensemble mean values H_e and x_e. We use a 10 m reference height z_r since it is the widely accepted value and is often the lowest level available from atmospheric models. Computing drag coefficients without knowing the orientation of obstacles brings with it its own uncertainty and the Garbrecht et al. (2002) parameterization accounts for this problem by reducing the form drag by a factor of $2/\pi$ given the assumption that obstacles are oriented randomly (Mock et al., 1972). An uncertainty of roughly $\pm 20\%$ is introduced on account of this assumption (Castellani et al., 2014). Lastly, to simplify further, we estimate the atmospheric neutral drag coefficient C_d^n only and do not consider the stability correction. The effect of the latter on form drag is explained in Birnbaum and Lüpkes (2002) and in more detail by Lüpkes and Gryanik (2015). With all the caveats taken into account and the integral having been evaluated we get the equation as presented in (Castellani et al., 2014):

$$C_{d,10,f}^n = \frac{c_w H_e}{\pi x_e} \frac{[\ln(H_e/z_0) - 1]^2 + 1 - 2(z_0/H_e)}{[\ln(10/z_0)]^2} \qquad (3)$$

Averaged obstacle height H_e and spacing x_e are the two parameters that are extracted from the ICESat-2 sea ice height data as mentioned in the section before. The coefficient of resistance c_w is computed as a function of obstacle height $0.185 + 0.147 H_e$ where 0.147 is in m^{-1} since the coefficient is unitless. The roughness length z_0 is kept at 1×10^{-5} m as derived from the aircraft measurements that were used to validate to the formulation in Garbrecht et al. (2002). As the roughness length is the height at which the wind speed becomes zero in the absence of wind-slowing obstacles and under neutral conditions, it can be generalized for smooth ice but nevertheless has its own associated uncertainty. With the form drag accounted for, we add the skin drag $C_{d,10,s}$ so as to calculate the total neutral atmospheric drag coefficients (Arya, 1973, 1975). We use the definition for skin drag proposed by Garbrecht et al. (2002) that is derived by use of the stability corrected logarithmic wind profile which gives skin drag as

$$C_{d,10,s} = \left[\frac{\kappa}{\ln(10/z_0)} \right]^2 \qquad (4)$$

and equates to 8.38×10^{-4}. Here $\kappa = 0.4$ is the von Kármán constant.

It is important to note that equation 2, and by extension equation 3, are only valid with the assumption of obstacle spacing being large enough such that the flow can return to its undisturbed state in between obstacles (Garbrecht et al., 2002). In Garbrecht et al. (2002), although the critical value of $H_e/x_e = 0.015$ for which this condition is satisfied was exceeded by the observed aspect ratio, the parameterization that accounts for this effect (Hanssen-Bauer and Gjessing, 1988) was neglected since the resulting form drag $C_{d,10,f}$ was changed by less than 3%. Similarly, in Castellani et al. (2014), including the

sheltering effect leads to a modification of less than 0.05% of the total drag coefficient. In this study, the sheltering function

220   $(1 - \exp(-0.5 x_e/H_e))^2$ (e.g., Hanssen-Bauer and Gjessing, 1988; Lüpkes et al., 2012; Castellani et al., 2014) is multiplied by OIB ATM-derived form drag coefficient estimates (derived via equation 3) but not ICESat-2 ATL07 data since due to the smoothing effect overestimating obstacle spacing (discussed further in section 3), the aspect ratio ends up being predominantly less than 0.015 Arctic-wide for ICESat-2.

2.5   Calculating total neutral drag coefficient

225   As the last step in our study, we also included the open water drag $C_{d,ow}^n$ and form drag due to floe edges $C_{d,e}^n$. $C_{d,ow}^n =$ $1.5 \cdot 10^{-3}$ is prevalent where there is open water and is therefore multiplied by $(1-A)$ where A is the sea ice concentration. $C_{d,e}^n$ is implemented using the Lüpkes et al. (2012) floe edge parameterization, wherein a constant $C_{d,e}^n = 3.67 \cdot 10^{-3}$ is multiplied with a function of sea ice concentration $A(1-A)$ that peaks at 50% signifying the MIZ. We use sea ice concentration from the AMSR2 microwave radiometer at $6.25\,\mathrm{km}$ grid resolution based on the ASI algorithm (Melsheimer and Spreen, 2019; Spreen

230   et al., 2008). The combined equation for the neutral $10\,\mathrm{m}$ sea ice–atmosphere drag, taken from Petty et al. (2017), is then as follows

$$C_{d,\mathrm{T}}^n = (1 - A)C_{d,ow}^n + AC_{d,s}^n + A(1 - A)C_{d,e}^n + AC_{d,o}^n \qquad (5)$$

where $C_{d,o}^n$ is the form drag due to obstacles calculated from ICESat-2 elevation data with equation 3, $C_{d,s}^n = 8.38 \cdot 10^{-4}$ is the skin drag originally calculated using equation 4, and all terms are referenced to a height of $10\,\mathrm{m}$. Equation 5 is evaluated on

235   daily ICESat-2 ATL07 tracks and we match daily ASI sea ice concentration maps to the ICESat-2 ATL07 tracks for the given day to ensure consistent sampling approaches from the different data-sets.

3   Results and discussion

The four-step process explained in section 2.3 is evaluated on sample near-coincident OIB ATM data (A,B) and ICESat-2 ATL07 data (C) in Fig. 1. Local maxima are found and those below the threshold of 20 cm (marked with a red dashed line

240   in the figure) are omitted (maxima that above the threshold are marked with a filled in black circle in the figure). Thereafter, the Rayleigh criterion is evaluated (those that fulfil the criterion are marked with a yellow 'x'). That is why we see a lot of unmarked black circles on the side of obstacles, because the Rayleigh criterion assures that only the maximum of the whole feature is considered (most clearly visible in Fig. 1A). Figs. 1A and 1B both depict the same 1 km long ATM segment from an OIB flight carried out on the 19th of April, 2019. The segment chosen is along the 88th parallel north and spans the longitude

245   range 170.60-170.85°E, putting it firmly within the central Arctic. The difference between Figs. 1A and 1B is that 1B has a moving average filter of box size 30 m applied. This is done to simulate the 30 m ICESat-2 ATL07 footprint (see section 2.1) which, as a result of the dual-Gaussian fit needed to reduce vertical uncertainty, also in effect smooths out the topography. For a more detailed description and case study of this smoothing effect, the reader is referred to the publication by (Ricker et al., 2022). Once the topography data is smoothed using this 30 m box filter, small clusters of narrow obstacles are viewed as one
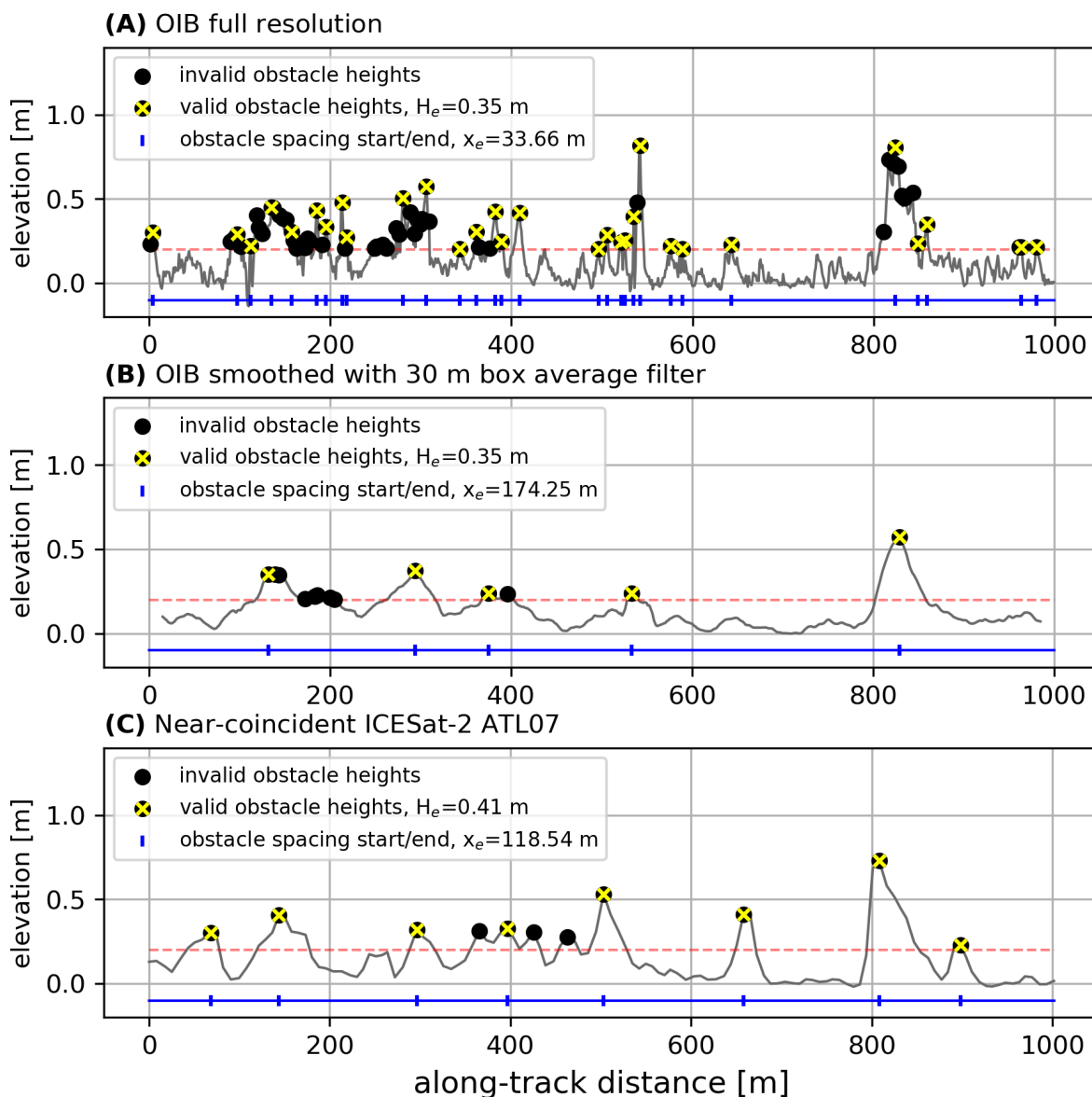
Figure 1. (A) Sea ice feature statistics from a sample OIB ATM flight on 19 April 2019 ($\sim$170.7°E, 88.0°N). (B) Same as (A) but smoothed to the ICESat-2 resolution via a moving average filter with box size of 30 m. (C) Sea ice feature statistics from a near-coincident ICESat-2 ATL07 track section. Black dots: all identified maxima; yellow 'x': maxima which satisfy the Rayleigh Criterion; red dashed line: 0.2 m threshold; blue line with dividers: identified obstacle spacing. All data is referenced to level ice (mode).

250 and the average distance between them for a given length scale is enlarged. In the case presented, average obstacle spacing x_e increases by a factor of ~5.2. Average obstacle height H_e comes out at 0.35 m for both plots. While the maximum obstacle height is larger in the original data, the smoothed data also has a smaller number of shorter obstacles that bring down the average. In general, we expect the height of tall narrow ridges to be underestimated due to sampling however. We can observe the smoothing effect in Fig. 1C wherein near-coincident ICESat-2 ATL07 data, with its low spatial resolution relative to OIB

255 ATM, also exhibits larger average obstacle spacing (factor of ~3.5) and therefore lower drag coefficient. As Fig. 1 covers only a small distance of 1 km to demonstrate the obstacle peak finding method, values presented are likely not representative of all data.

3.1 Drag coefficient regression with airborne lidar measurements

Taking the spring 2019 OIB/ICESat-2 underflights (4 days in 2019) that were near-coincident with the measurements of
260 ICESat-2, we can calculate drag coefficients from both data sets and compare the results. The shortest time-lag during the underflight was less than 1 min for 3 of the flights (8, 12 and 19 April 2019) (Kwok et al., 2019a), however, 8 and 12 of April are overlapping racetracks conducted for a time period of ~8 hours, thus the time-lag is highly variable (all legs were considered to maximize the total amount of data). The shortest time lag on April 22, also used for this comparison, was ~38 min (Kwok et al., 2019a). We used a subset of all OIB data that fell within the specified azimuthal angle range of the ATM scanner
265 which likely reduced the spatial coincidence as well. As a result, we did not simulate a one to one elevation comparison as has already been done in Kwok et al. (2019a) and Ricker et al. (2022) and thus did not employ any drift correction. Since we look at 10-km averages for the purpose of comparing regional average form drag, it was sufficient to compare averaged data of similar ice regimes and not focus on the coincidence itself. Since the averages are not aligned, the data-sets are gridded to a 12.5 km grid and the comparison takes place between matching filled in grid cells (see Fig. 2).

270 Thus Fig. 2 shows a comparison between form drag coefficients calculated from ICESat-2 ATL07 and OIB ATM segments (blue). As expected, the majority of form drag coefficients calculated from OIB ATM occupy a wider range ($\sim 03 - 1.3 \cdot 10^{-3}$) than their ICESat-2 ATL07 grid cell counterparts ($\sim 0 - 0.3 \cdot 10^{-3}$). As shown in Fig. 1, we can simulate ICESat-2 ATL07 by passing all OIB ATM data through a moving average filter of varying box sizes (15 m, 30 m and 45 m) and observe that we can get the line of best fit to match the one-to-one line depending on the size of the averaging box (Fig. 2). Smoothing with a
275 box size of 30 m, which is comparable to the ATL07 strong beam ~ 30 m spatial resolution (Kwok et al., 2019b), results in a line of best fit that is the closest match to the one to one line, which is encouraging.

The beam used for model training is the second strong beam as it is in best spatial agreement with all 4 OIB ATM flight near-coincident data (Kwok et al., 2019a). Using the line of best fit from Fig. 2 (in blue) we correct the ICESat-2 ATL07 form drag coefficients towards the OIB ATM form drag coefficient range as

280 $$C_d^{mod} = 6.24 C_d + (1.5 \cdot 10^{-4}) \qquad (6)$$
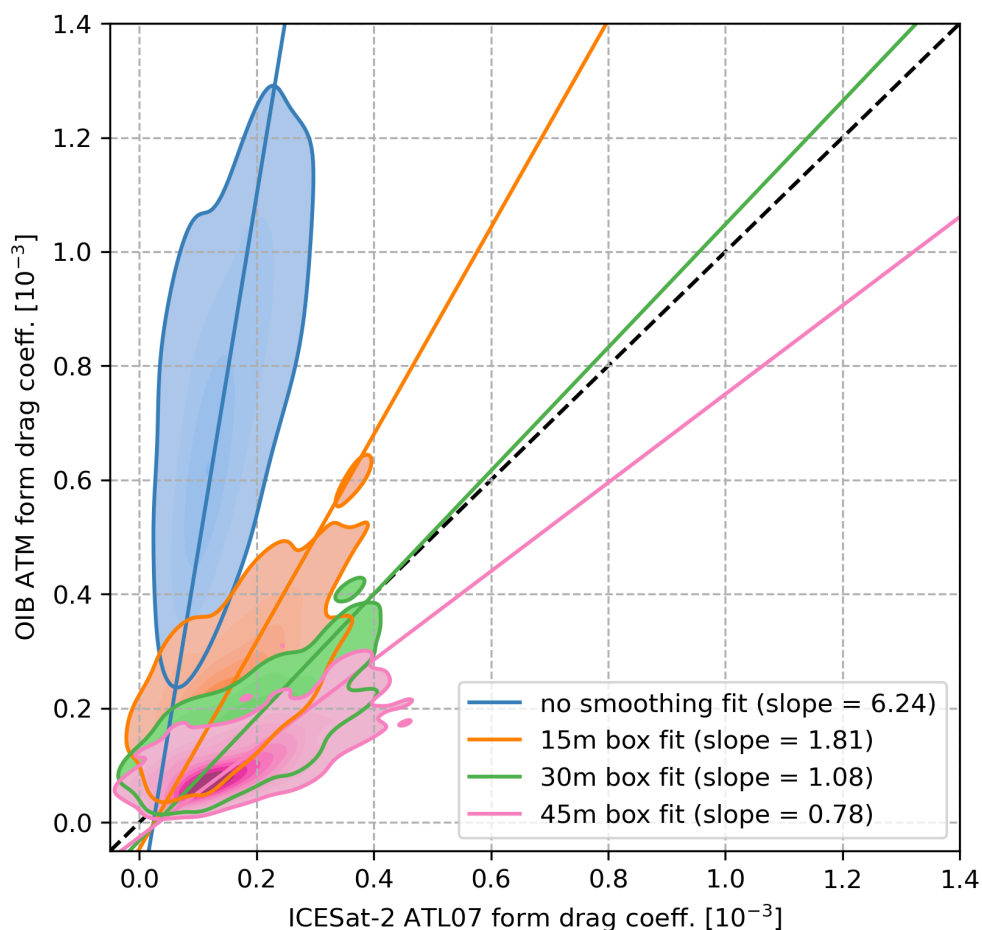
Figure 2. Heat maps of 12.5 km grid resampled 10-km average ICESat-2 ATL07 form drag coefficients plotted against those computed from OIB ATM drag coefficients from 4, 8, 19 and 22 April 2019; resampled and calculated in the same manner (in blue) as well as the OIB ATM data smoothed by a moving average filter with a window sizes of 15 m (in orange), 30 m (in green) and 45 m (in pink). The lines represent Huber fits with colour coding matching that of the bivariate heat maps; except for the dashed black line which represents the identity line.
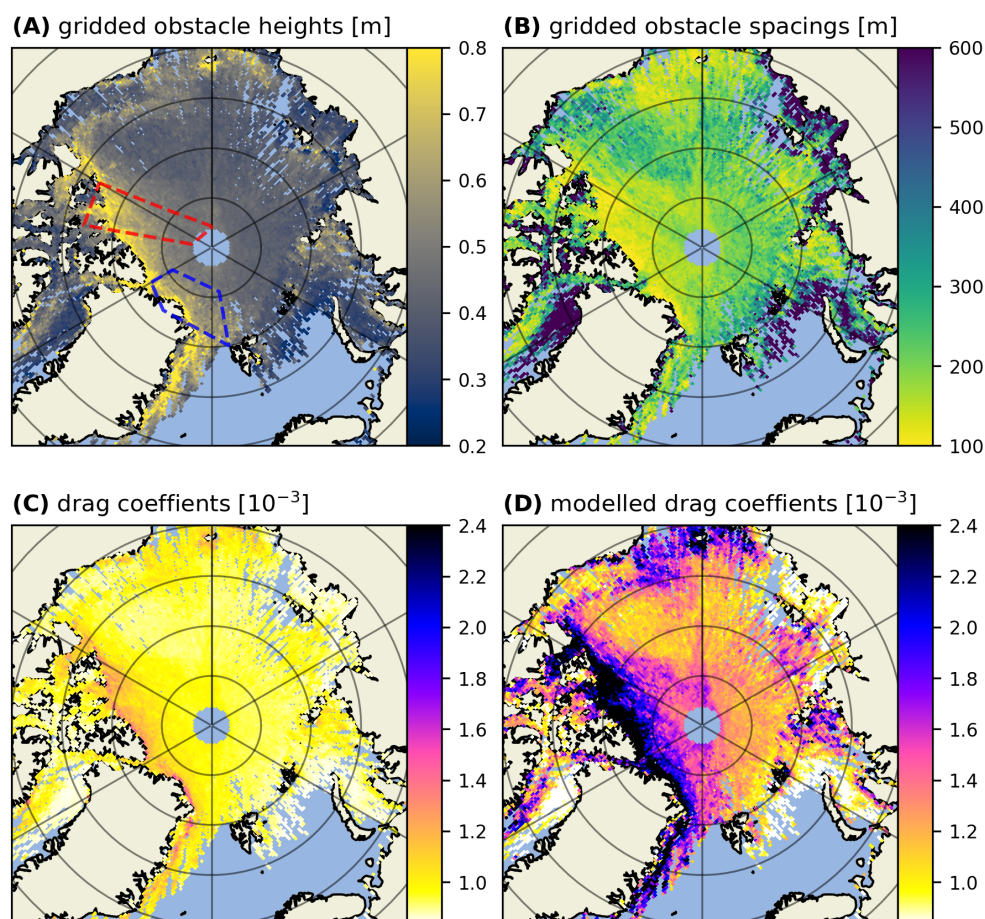
Figure 3. Data computed from April 2019 ICESat-2 ATL07 tracks (all three strong beams): (A) average obstacle height, (B) average obstacle spacing, (C) total neutral 10-m atmospheric drag as computed from ICESat-2 average obstacle height and spacing, (D) total neutral 10-m atmospheric drag as computed from ICESat-2 average obstacle height and spacing with the OIB ATM regression model applied. In (A) zones marked in red and blue represent near-coincident OIB ATM topographic data used to generate the regression model (08, 12, 19, 22 April 2019) and data used for evaluation (06, 20 April 2019), respectively.

For an inter-comparison of the drag coeffients processed for each of the three strong beams see Fig. A2 in A. Using the first and third strong beams we can produce a similar result despite the model being trained with the second strong beam (the most coincident beam). To incorporate the full available high-resolution data-set as well as minimize random sampling errors from here on we use all three strong beams for all ICESat-2 ATL07 parameter maps.

285   In Fig. 3 we map average obstacle height and spacing used as input in equation 3 as well as the resulting total atmospheric drag coefficient for the month of April, 2019. The areas outlined in Fig. 3A represent the area where near-coincident OIB ATM flights took place (in red) as well as additional topographic data over sea ice from the month of April 2019 (06.04 and
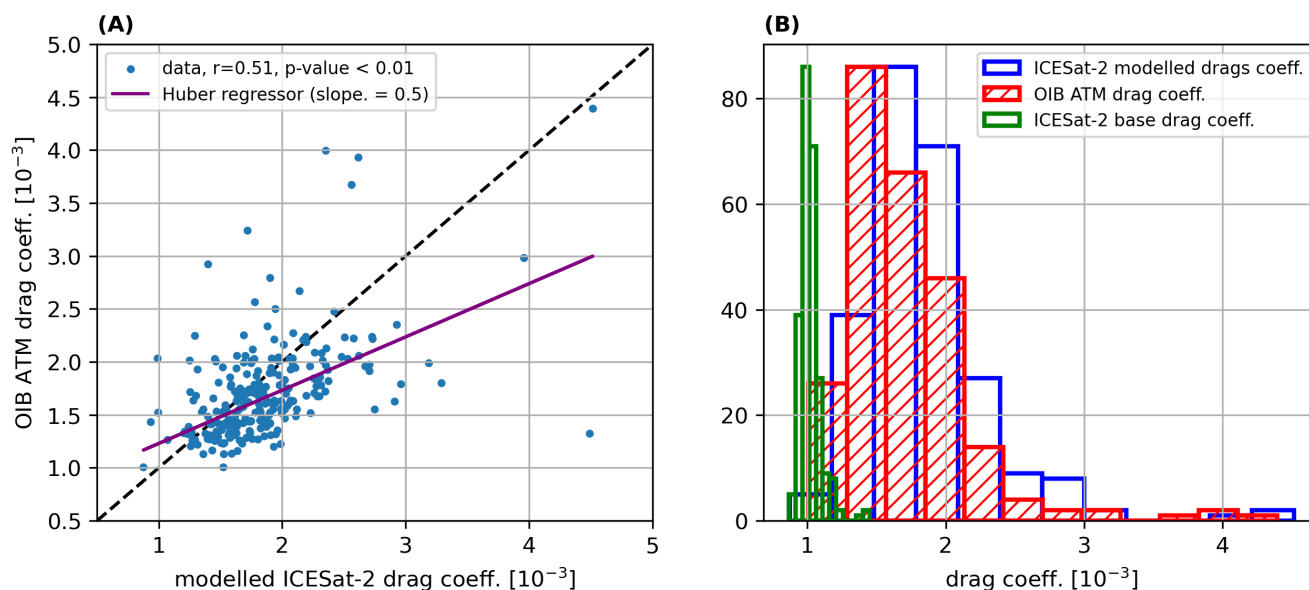
Figure 4. (A) Scatter plot of the scaled up ICESat-2 ATL07 drag coefficients from April 2019 plotted against OIB ATM drag coefficients from 6 and 20 April 2019; resampled and calculated in the same manner. (B) Histograms of ICESat-2 ATL07 drag coefficients with (in blue) and without (in green) the regression model applied as well as the OIB ATM drag coefficients (in red) wherein all three data-sets are distributed among 12 bins (i.e., with varying bin size).

20.04) that is used for the evaluation study in section. 3.2 (in blue). Looking just at the drag coefficients, in Figs. 3C and 3D, we can see that with the OIB ATM regression model applied, the data product is in much better agreement with the pan-Arctic maps produced in Petty et al. (2017) as well as the regional drag assessments conducted in Castellani et al. (2014). The spatial variability across all parameters in Fig. 3 also confirms the expectation of multiyear ice that is predominantly north of Greenland and the Canadian Archipelago being more rough ($C_d > 1.2 \cdot 10^{-3}$ before scaling up; $C_d > 2.2 \cdot 10^{-3}$ after) and as a consequence exhibiting a higher concentration of tall ridges ($H_e > 0.8$ m) and thereby shorter spacing ($x_e < 100$ m) between them.

3.2 Evaluation study

We take advantage of OIB data from north of Greenland (outlined in blue in Fig. 3A) and collocate it to ICESat-2 ATL07 drag coefficient data produced for the month of April 2019 to perform an evaluation study of our product. In Fig. 4A, we compare the drag coefficients computed from the OIB ATM data-set using the methods (see section 2.3) that were used on the near-coincident 'training' data-set (outlined in red in Fig. 3A), to matching grid cells from the 2019 ICESat-2 ATL07 drag coefficient map that has been scaled up by the OIB ATM regression model (Fig. 3D). Correlation (0.51) and slope (0.5) of the bivariate distribution is reasonable and presumably not any higher since the two data-sets are retrieved on different days with ice drifting

in between, but still positive suggesting some base similarity in the local spatial variability of surface drag. In Fig. 4B we also include the ICESat-2 ATL07 drag coefficients prior to the upscaling step (in green); where all three data-sets of equal size are divided among 12 bins. Here we use narrower bins for the base ICESat-2 ATL07 drag coefficients so as to keep the height of all histograms identical for viewing purposes. Notably, the distribution of the base drag coefficients is overall much narrower than the other two with the main peak centered around $\sim 1.0 \cdot 10^{-3}$ and a secondary peak at $\sim 1.4 \cdot 10^{-3}$. Meanwhile, the distribution of OIB ATM and scaled up ICESat-2 ATL07 drag coefficients both show a similar distribution with the main peaks centered around $\sim 1.5 \cdot 10^{-3}$ and a smaller secondary peaks at $\sim 4.0 \cdot 10^{-3}$. This suggests that our scaled up ICESat-2 ATL07 drag coefficients perform reasonably well to represent the drag variability, at least for this part of the Arctic. If further ATM data becomes available from different regions in the Arctic this evaluation should be extended.

3.3 Interannual drag coefficient estimates

To increase the temporal coverage of Fig. 3, we look at spatial variability in 3-month aggregates throughout 2019 in Fig 5 (see Figs. A3 and A4 in A for years 2020 and 2021). Here 3 months are chosen to be a reasonable time-frame to maximize the data contained within individual maps on account of ICESat-2's 91-day repeat cycle (e.g., Kwok et al., 2021a, 2019b). All rows of maps within Fig. 5 contain obstacle height, spacing and drag coefficient for consecutive three-month periods.

In the last column (col. IV), we include the floe edge and open water drag coefficient terms according to equation 5; there we can observe drag coefficients $> 1.5 \cdot 10^{-3}$ along the MIZ. This combined parameterization is our best estimate for satellite derived atmosphere-ice drag. It includes variable form drag due to obstacles and floe edges as well as constants for open water and ice skin drag. However, drag due to floe edges next to over-frozen leads as well as at the edges of melt-ponds in summer is not accounted for (which could be a future enhancement). By looking at the full year separated into 3-month aggregates we can observe the spatio-temporal evolution of drag coefficients Arctic-wide. We observe a seasonal variability of up to $\pm 1.0 \cdot 10^{-3}$ in some multiyear ice regions though there is a thin band of ice close to the Canadian archipelago that is consistently $> 2.0 \cdot 10^{-3}$. Arctic-wide, this effect is comparatively smaller, but nevertheless a change of up to $\pm 0.5 \cdot 10^{-3}$ in total drag coefficient occurs in most areas of the Arctic. This is consistent for the years 2020 and 2021 as well (see Figs. A3 and A4 in A).

For both columns III and IV in Figure 5 it is important to mention that the summer months likely exhibit higher levels of uncertainty, e.g., due to data gaps caused by clouds and due to melt ponds that can saturate the ICESat-2 photon detection system (Tilling et al., 2020). This is a consequence of melt ponds being highly specular and typically reflecting a large amount of signal photons. When ATLAS strong beam timing channels receive more photons than they can handle within a dead time interval, they can no longer detect additional incoming photons; which can lead to short gaps in the topography data. See Tilling et al. (2020) for more information on how ICESat-2 views melt ponds.

To observe the seasonality as well as the monthly evolution of our best estimate of pan-Arctic total neutral drag coefficients on an interannual scale from November 2018 to June 2022, we plot the average drag coefficient, obstacle height and spacing for each month along with the total area of grid cells covered with ICESat-2 data (note that this area is smaller than the actual Arctic sea ice area) in Fig. 6. Notably, both obstacle height and spacing is what is used to calculate the base ICESat-2 ATL07 drag coefficients; for these no corrections are applied and thus it is expected that the heights are underestimated and the
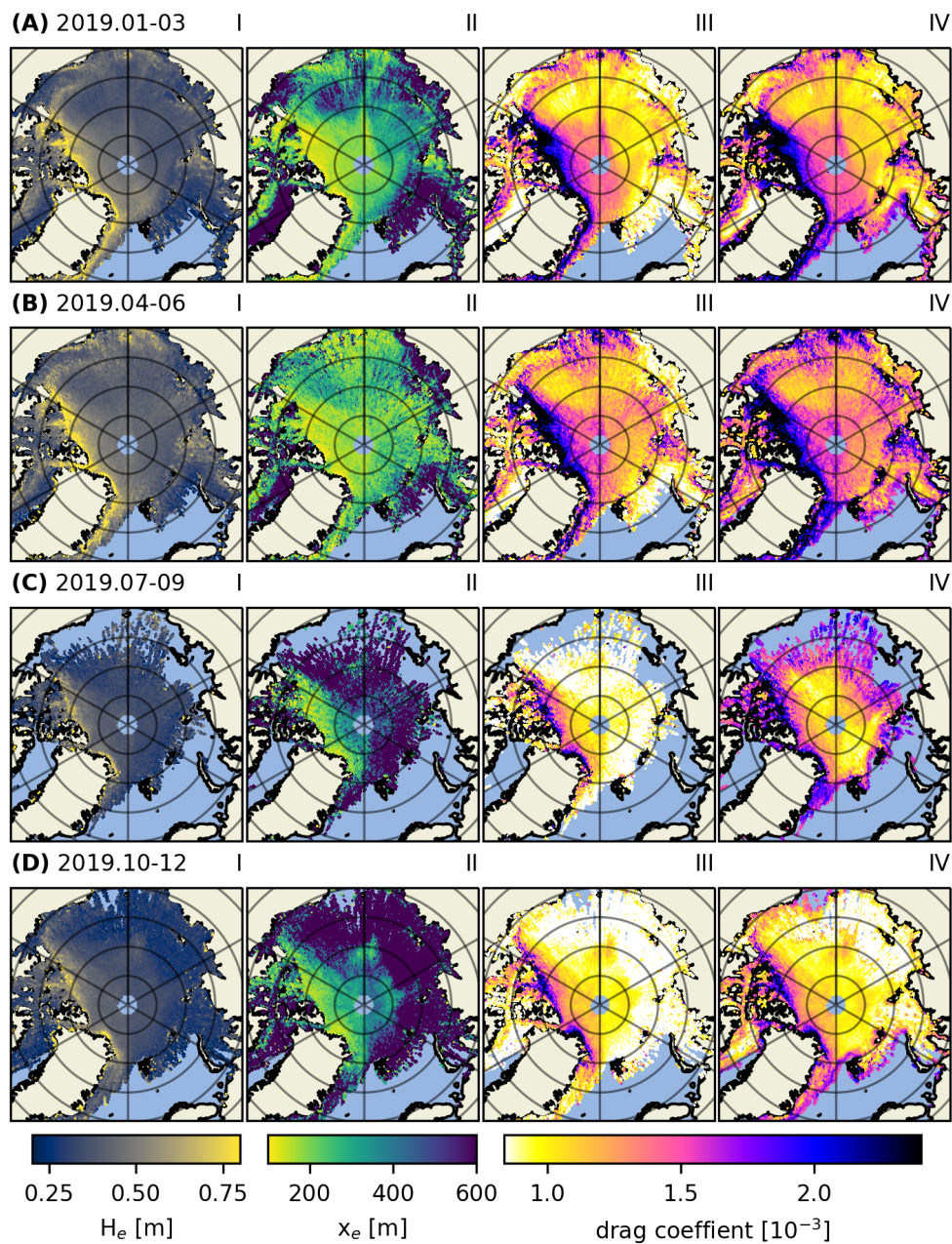
Figure 5. 2019 obstacle height (I), obstacle spacing (II), drag coefficient as a sum of sea ice skin drag and form drag due to obstacles (III), total drag coefficient as a sum of the sea ice skin drag, form drag due to obstacles and floe edges and open water drag (IV). Importantly, columns I and II are the the obstacle heights and spacings as retrieved from ATL07, whereas in columns (III) and (IV) the form drag due to obstacles is scaled up using the OIB ATM regression model. The periods for which these parameters are calculated are January to March (A), April to June (B), July to September (C) and October to December (D), 2019.
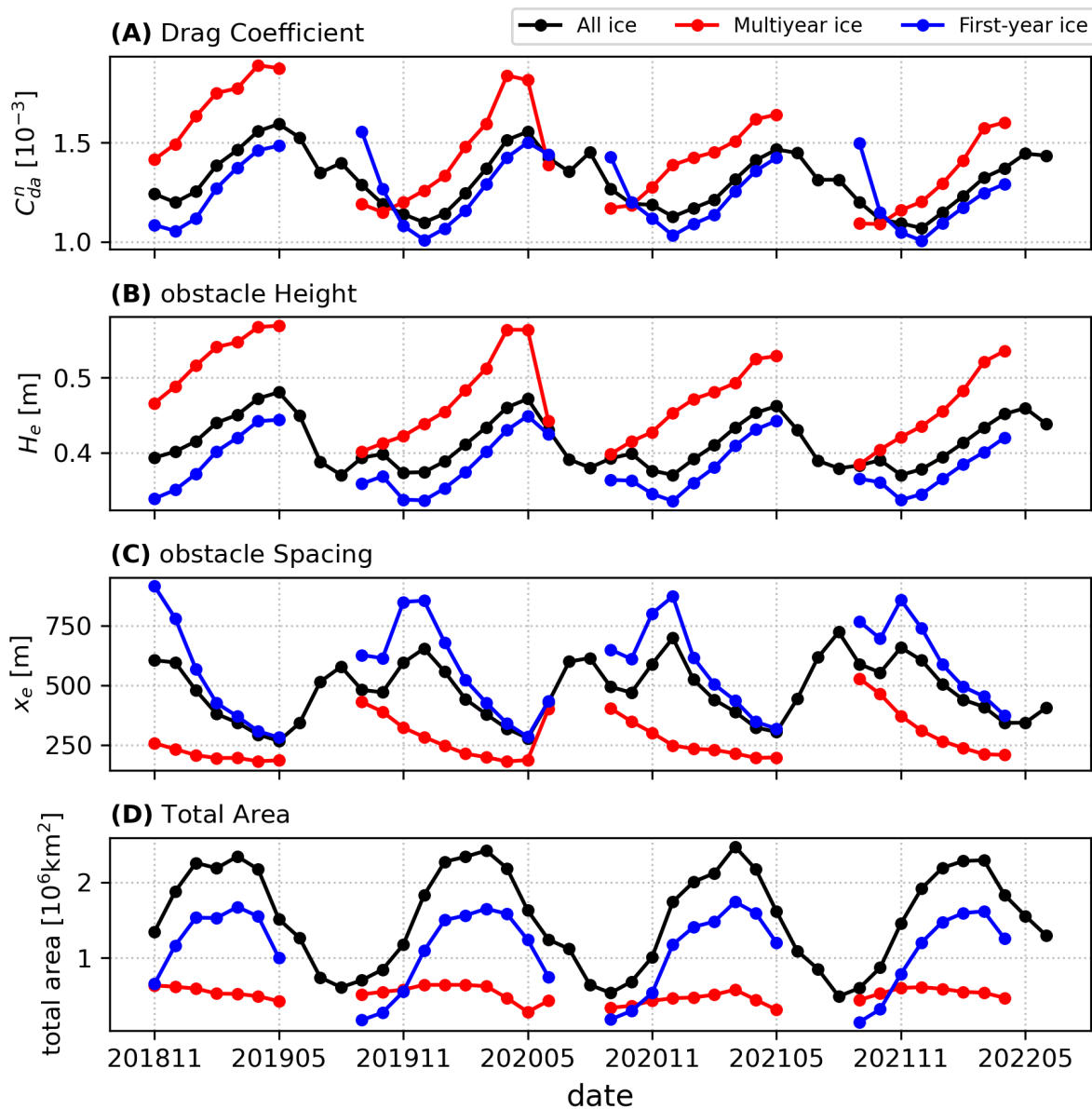
Figure 6. Time series from 11.2018 to 06.2022 of total ICESat-2 drag coefficient (as computed in equation 5) with the OIB ATM regression model applied (A), obstacle height (B), obstacle spacing (C) and total area covered by ICESat-2 observations (D) for the whole Arctic (in black), multiyear ice (in red) and first-year ice (in blue).

spacing overestimated as compared to OIB ATM due to smoothing by the larger ICESat-2 footprint. In addition to pan-Arctic averages, we also produce these statistics for multiyear ice (MYI) and first-year ice (FYI). Here, we make use of the MYI concentration retrieved using brightness temperatures from the microwave radiometer AMSR2 and radar backscatter from the C-band scatterometer ASCAT (Shokr et al., 2008; Ye et al., 2016a, b; Melsheimer et al., 2022). Sea ice area classified as below

340   50% MYI according to the retrieval, are considered as FYI and used to compute FYI averages and conversely all values equal to and above 50% are used to compute MYI averages. By comparing the two ice types we can study the differences in their areal averages. As expected we see higher drag coefficients (MYI: $C_d \approx 1.2 - 2.0 \cdot 10^{-3}$, FYI: $C_d \approx 1.0 - 1.6 \cdot 10^{-3}$) and obstacle heights (MYI: $H_e \approx 0.4 - 0.6$ m, FYI: $H_e \approx 0.3 - 0.4$ m), and conversely lower obstacle spacings (MYI: $x_e \approx 200 - 500$ m, FYI: $x_e \approx 250 - 1000$ m) in the averages from the MYI ice portion of the Arctic. The MYI concentration data product is only

345   available for winter months and hence the lack of data for the summer months in the time series. As a result this means we are unable to distinguish the FYI contribution of the form drag due to floe edges peak in August and can only estimate that upper bound given the full data-set. As for temporal evolution, there is a annual cycle in all three parameters such that the annual maximum (minimum) average drag coefficient and obstacle height (obstacle spacing) in May lags behind maximum sea ice extent which is typically in March.

350   ## 3.4   Spatial and temporal variability

Looking at our 3-monthly spatial analysis (Figs. 5, A3 and A4) as well as the monthly time series (Fig. 6), we corroborate the results found in Petty et al. (2017) with the MYI sea ice regions north of the Canadian Archipelago and Greenland exhibiting high drag ($C_{d,10}^n > 1.5 \cdot 10^{-3}$) and the smooth FYI sea ice regions of the Beaufort, Chukchi and Siberian Seas exhibiting low drag ($C_{d,10}^n < 1.0 \cdot 10^{-3}$). We corroborate Duncan and Farrell (2022) in terms of the distribution of spatial variability of 10-km

355   average obstacle spacing, e.g., <200 m near the Canadian Archipelago, for the winters of 2019, 2020 and 2022 that they have produced using the UMD-RDA algorithm. Based on the limited amount of data we analysed, we also corroborate that the drag coefficient variability in space is larger than the variability across seasons as was found by others (Castellani et al., 2014; Tsamados et al., 2014).

We observed interesting features of ice topography, including a tongue of ($C_{d,10}^n > 1.5 \cdot 10^{-3}$) sea ice that forms across the

360   Beaufort Sea and towards a rough ice patch surrounding the Wrangel Island only in select months (see Figs. 5B and A4B). Similarly, when Arctic sea ice extends across the Arctic Ocean and to Siberia, Severnaya Zemlya is often (but not always) surrounded by rough ice as well ($C_{d,10}^n > 1.5 \cdot 10^{-3}$) (see Figs. 5B and A3B). These effects may be attributed to the movement of the Beaufort Gyre as well as to the tendency of ice to ridge near land, respectively. Notably, within the time span we analysed, May is the month that repeatedly exhibits annual minimum obstacle spacing and annual maximum obstacle height and drag

365   coefficient. This supports the notion that sea ice–atmosphere drag exhibits an annual cycle (e.g., Andreas et al., 2010). By also including drag due to floe edges we also observe a smaller peak in August, when the ice-water boundary is at its longest. We observe a decrease in the yearly maximum average drag coefficient across all ice types during the four years we looked at, but given the short time-frame we cannot attribute this decrease to anything more than natural variability.

3.5 Uncertainty due to sampling and resolution

370 While ICESat-2 has a very high resolution when compared with other laser altimeter satellites, it's still larger than the 1 m resolution of the OIB ATM data. The ATL07 segment length of about 30 m, over which 150 signal photons are obtained to lower noise in the height retrieval, smooths out the topography via the dual-Gaussian fit much like the moving average filter we applied to the OIB ATM data. This smoothing effect is discussed in detail in a recent study by Ricker et al. (2022) where coincident ICESat-2 ATL07 and airborne Altimeter Laser Scanner (ALS) data from the MOSAiC (Multidisciplinary drifting

375 Observatory for the Study of Arctic Climate) expedition were compared. Ricker et al. (2022) show that the ICESat-2 ATL07 strong beam could detect only 16% of obstacles above the threshold of 0.6 m that were registered by ALS. A comparatively higher detection rate of 42% was achieved by processing ATL03 by using a higher-resolution topography data-set (Duncan and Farrell, 2022). Notably, neither of the two ICESat-2 sea ice height products were able retrieve the full extent of surface topography (Ricker et al., 2022). Assuming the lower threshold value of 0.2 m used in this study, we can expect these detection

380 rates to rise but at some point hit a limit imposed by ICESat-2 ATL03's footprint of 11 m (Magruder et al., 2020, 2021) that is inferior to the resolution used in most modern airborne surveys looking at topography, e.g., OIB ATM, ALS. Thus for the purposes of our pan-Arctic study, we have chosen to stick with the publicly available and regularly updated ATL07 data-set as either of these two data products will require some type of correction if realistic drag coefficient estimates are to be computed from them. While ATL07 has a lower obstacle detection rate locally and the obstacle height (spacing) is typically

385 overestimated (underestimated), the spatial information on Arctic-wide obstacle distribution should be conserved according to our comparisons to airborne data (Section 3.1). That is why we use a regression transfer model that is trained by near-coincident OIB ATM to scale up these underestimated ICESat-2 drag values and obtain them closer to the expected form drag range estimated from higher-resolution airborne laser data.

3.6 Significance and novelty of the analysis

390 Using our best estimates, we have demonstrated that drag force between Arctic sea ice and the atmosphere varies annually throughout the year (see Fig. 6). The implication of this finding is that the turbulent surface flux of momentum, given in equation 1, varies also. In other words, depending on the month of the year, the ice is either more or less susceptible to movement depending on the amount of energy transferred to it via the atmosphere, and by extension, the ocean. We include the ocean here because the sources of atmospheric drag we looked at, primarily form drag due to obstacles, are closely related

395 to the magnitude of oceanic form drag on account of pressure ridges having both a sail (the part above water) and a keel (the part below water) in roughly the same location (Timco and Burden, 1997; Tsamados et al., 2014). Similarly, form drag due to floe edges is also subject to energy transfer from the ocean for the majority of the ice edge that is below the water level. Thus both oceanic and atmospheric form drag are expected to be both temporally and spatially correlated to one another, wherein the oceanic drag is higher in magnitude (Tsamados et al., 2014). Form drag from meltpond edges, a parameter we did not look

400 at here, we expect to be a unique component of total atmospheric drag.

We observe that MYI ice exhibits highest drag in May (red line in Fig. 6A), due to an increase in the form drag due to obstacles, and FYI ice peaks sometime in July-August (blue line in Fig. 6A) from a longer ice-water edge and the associated floe edge drag in summer months. Looking at the gridded data (Figs. 5, A3 and A4), we can further comment on developments on regional scales. Notably it is the Lincoln Sea, north of Greenland, which exhibits the highest form drag due to obstacles
405 with high drag coefficients (2-3x higher than smooth FYI areas, e.g. the East Siberian Sea) reaching as far north as 85 deg in the months of spring (rows A and B). However this is not consistent throughout the year as these relatively high drag coefficients tend to retreat towards the Canadian archipelago throughout summer and autumn (rows C and D). Interestingly, it is not consistent across all years either as this behaviour was not observed in 2021 (Fig REF). Similarly, the neighbouring Beaufort Sea and Fram Strait (mixture of MYI and FYI) also exhibit wide areas of higher form drag coefficients sometime in
410 late spring (row B). All other Arctic Seas (mostly FYI) primarily show an increase in form drag due to floe edges along the MIZ (see column IV), but also in small part higher form drag due to obstacles near land features. Thus, this data proves highly valuable in terms of identifying previously unknown spatial and temporal developments in pan-Arctic and regional drag. This analysis is the first of its kind as previous studies either assumed uniform drag across the Arctic or did not provide sub-yearly temporal information.

415 In terms of climate modelling, our findings show that assuming a constant drag coefficient in both space and time misrepresents the variability of momentum fluxes near the surface and thus the main forcing of sea ice drift. This misrepresentation might cause in turn many other deficiencies in air ice interaction such as insufficient variability in the sea ice concentration. Accordingly, a suitable further development of drag parameterizations for a more realistic representation of form drag seems necessary. As for understanding Arctic sea ice, we believe this data has the potential to help with better understanding the
420 interaction between sea ice, ocean and atmosphere, better predict the motion of sea ice and identify temporal and spatial variability of pan-Arctic drag coefficients on a monthly basis. Most importantly, this study helps us link yet another crucial sea ice parameter to remote sensing. This link, given ICESat-2 or similar future mission data is available for years to come, has the potential to help us better understand the multiannual changes in Arctic sea ice cover as the local climate warms at an unprecedented pace (e.g., Serreze and Barry, 2011; Stroeve et al., 2012).

425 4   Summary and outlook

This study relates measured sea-ice topography to atmospheric drag coefficients across the Arctic ice cap on monthly and 3-monthly temporal scales. To our knowledge, it is the first analysis of monthly pan-Arctic drag coefficient estimates of its kind. The sea-ice topography is obtained from the ICESat-2 ATL07 data product at variable resolutions that depend on surface reflectivity but average around 30 m for the strong beams (Kwok et al., 2019b). Using methods developed in Garbrecht et al.
430 (1999) and Garbrecht et al. (2002) according to the drag partitioning scheme proposed by Arya (1973, 1975), we obtain obstacle, i.e. ridges, height and spacing averages for 10-km segments. We then combine the estimated form drag due to obstacles with sea ice skin drag, drag due to floe edges and a drag due to open water; all of which are incorporated as constants scaled differently with sea ice concentration.

In conclusion, from our analysis of pan-Arctic drag coefficients from the year 2019 and to a lesser extent 2018, 2020, 2021
435   and 2022, we have observed several noteworthy natural phenomena. Pan-Arctic form drag due to obstacles follows an annual
cycle that is similar in both MYI and first-ice regions. The yearly maximum average drag coefficient is not connected to the
yearly maximum sea ice extent and seems to occur after the sea ice extent maximum. Form drag due to obstacles is primarily
spatially variable (high in MYI regions and low in FYI regions) but nevertheless shows some temporal variability (Maximum
in May and minimum in December). Our results suggest that form drag due to floe edges is more prevalent during summer
440   months when large areas are broken up and the MIZ expands, whereas form drag due to surface features peaks in late spring
when its contribution is magnified from MYI regions north of the Canadian Archipelago and Greenland.

While it is beyond the scope this study, we propose the possibility of extending ICESat-2-based analysis to also estimate form
drag due to floe edges and the freeboard variability thereof rather than using a constant. For this task we propose making use of
the ATL10 sea ice freeboard data product. We encourage the open water drag component to be derived from a parameterization
445   that takes into account wind speed and therefore wave height that might cause additional form drag across water surfaces. We
propose the use of lead and meltpond data to account for additional sources of drag not included in our study, e.g. lead and
meltpond edges.

Data availability. The AMSR2 ASI Sea Ice Algorithm sea ice concentration data product Melsheimer and Spreen (2019); Spreen et al.
(2008) and AMSR2 / ASCAT Multiyear ice concentration data product Shokr et al. (2008); Ye et al. (2016a, b); Melsheimer et al. (2022) are
450   used from local repositories and publicly available at https://seaice.uni-bremen.de/data-archive/.

NASA ICESat-2 ATL07 sea ice height (version 5) data product is obtained from https://doi.org/10.5067/ATLAS/ATL07.005, Kwok et al.
(2021b). NASA OIB ATM L1B elevation data product (version 2) is obtained from https://doi.org/10.5067/19SIM5TXKPGT, Studinger
(2013).

The processed data files used to produce the figures in this research can be found on Pangaea Mchedlishvili et al. (2022).

Appendix A: Supporting Figures

Using our methods, we obtain a sufficient amount of data to mostly fill a polar-stereographic 25 km grid via bucket resampling
for each month to produce a pan-Arctic monthly total neutral atmospheric drag coefficient analysis. On account of ICESat-2's
near-polar orbit the data density is highest around the pole hole and wanes at lower latitudes (see Fig. A1A). As a result, the
regional drag coefficient estimates at higher latitudes are more representative of the time period shown in Figs. 3, 5, A3 and
460   A4, whereas those at lower latitudes are computed with height measurements from select days. However, mind that we do not
see any discontinuities due to variable sampling in the final atmosphere-ice drag maps. In Fig. A1B one can observe the typical
spacing between ATL07 height estimates, which is typically around around ∼11-13 m but can be higher due to dark surfaces
over which up to 200 m might be needed to collect the sufficient signal photons Kwok et al. (2021a). Similarly, clouds can also
increase the spacing as no measurements are retrieved beneath them.
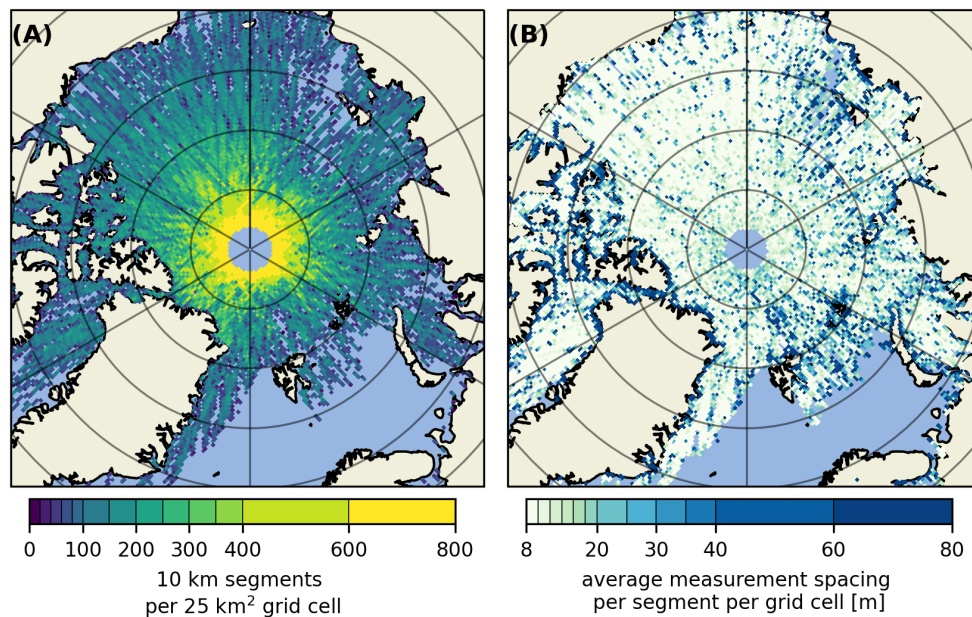
Figure A1. The data distribution for the 04.2019 drag coefficient map given as the number of 10 km segments from all strong beams per 25 km^2 grid cell (A). The average point spacing within each 10 km segment per 25 km^2 grid cell (B).

465   For a comparison between different beams, all of which we combine in our final data product, we refer the reader to Fig. A2. Inter-beam variability due to different range biases is present and was reported on by the ICESat-2 Project Science Office (PSO) in their preliminary analysis (e.g., Bagnardi et al., 2021). In addition, there is the 3.3 km inter-beam spacing which suggests ridges and snow features captured by one beam might not be captured by the rest. At first look Fig. A2D, the inter-beam standard deviation, suggests more variability in the MYI rough ice areas but that is because the OIB ATM regression

470   model applied to all data scales up all drag coefficients linearly, and hence the variability is increased in those areas as well.
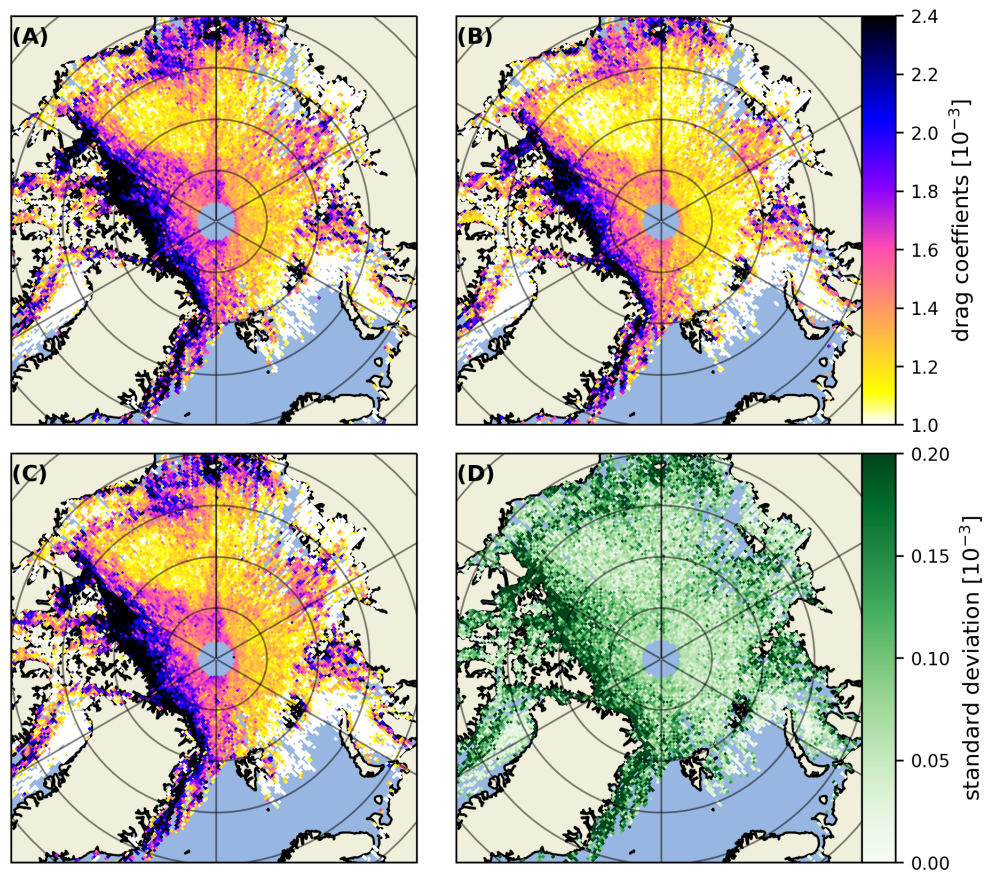
Figure A2. Comparison between drag coefficient estimates (sea ice form drag + skin drag) computed from the 1st (A) 2nd (B) and 3rd (C) strong beams as well as the standard deviation between them (D). All three examples have the OIB ATM regression model applied.
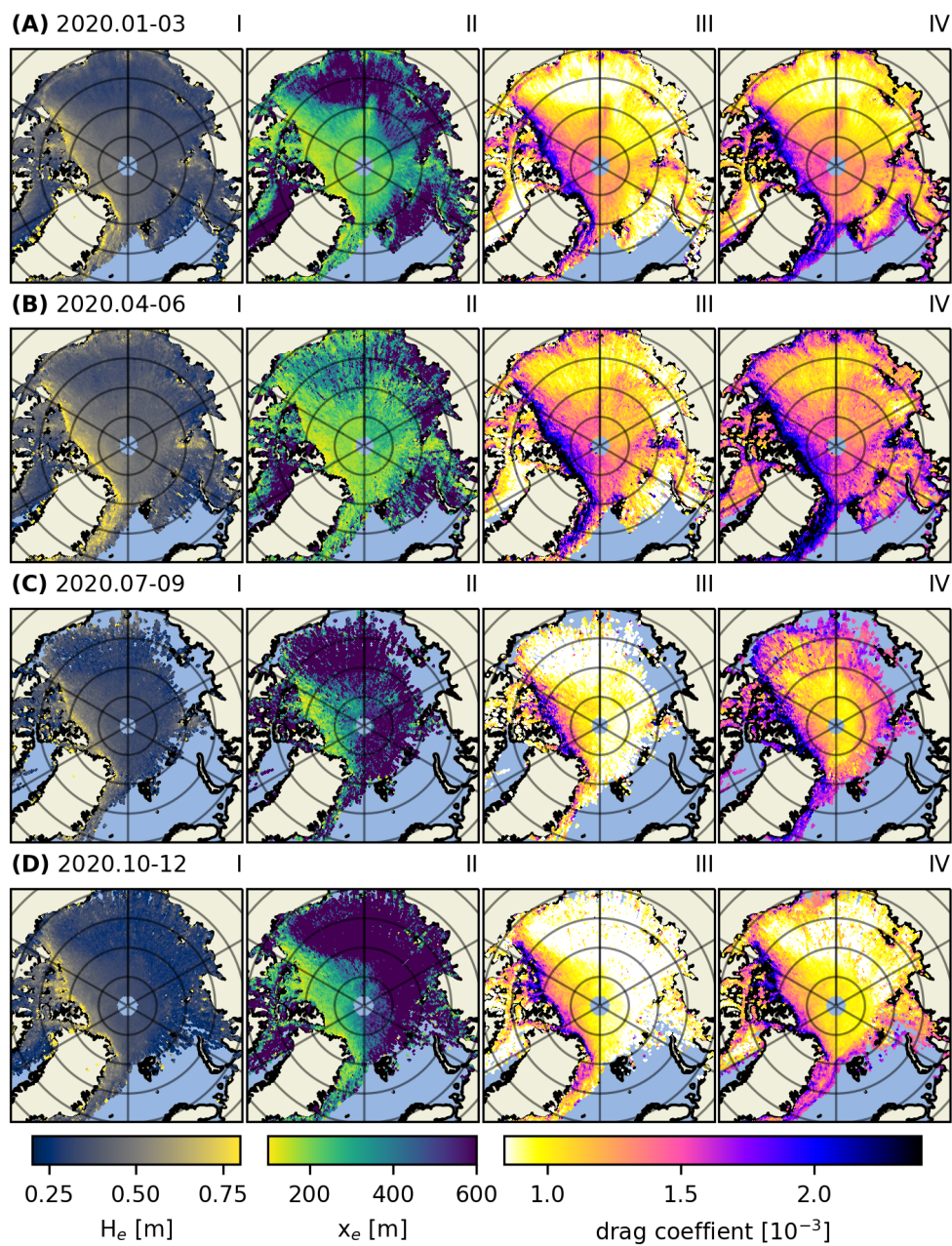
Figure A3. Same as Figure 5 but for 2020. Obstacle height (I), obstacle spacing (II), drag coefficient as a sum of sea ice skin drag and form drag due to obstacles (III), total drag coefficient as a sum of the sea ice skin drag, form drag due to obstacles and floe edges and open water drag (IV).
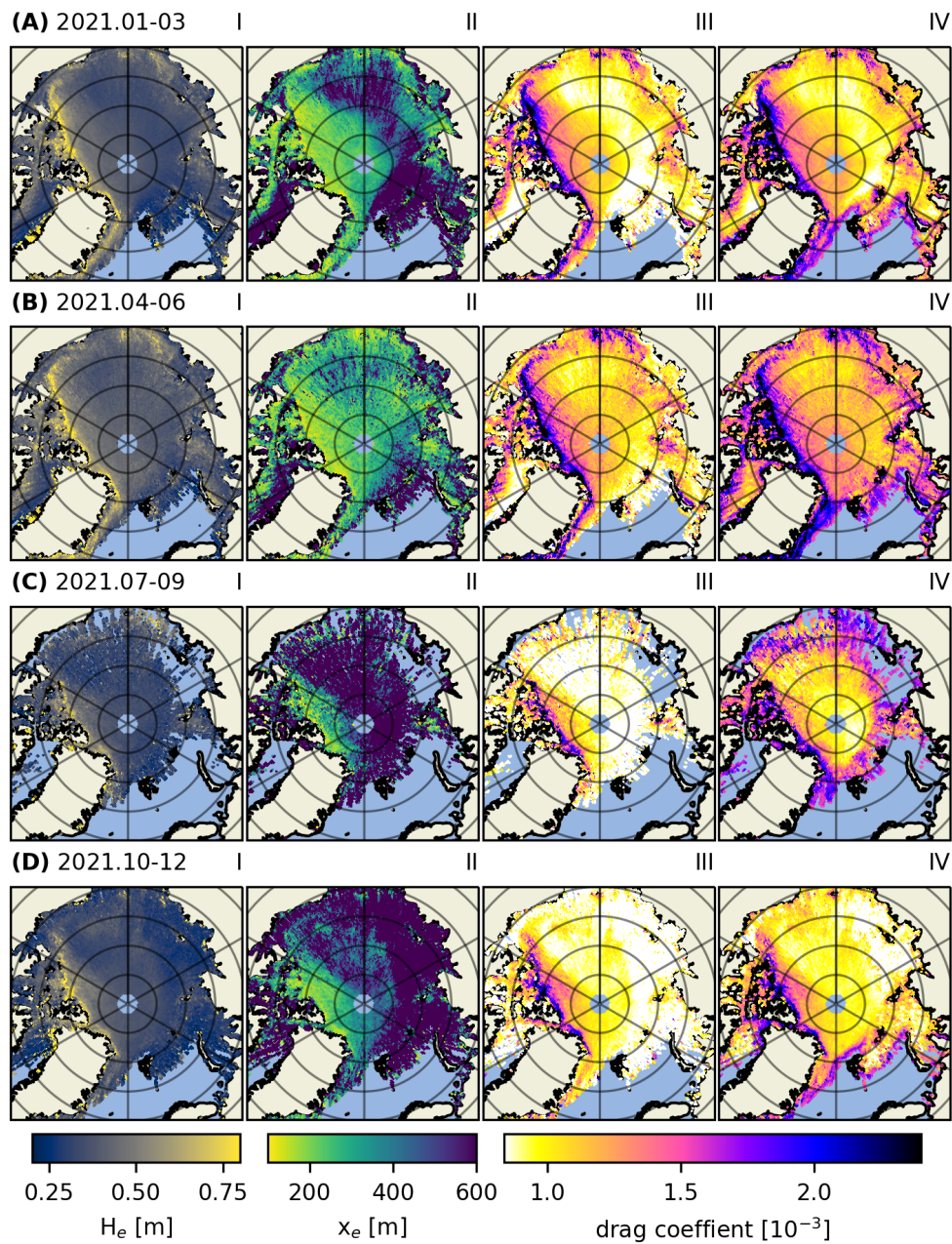
Figure A4. Same as Figure 5 but for 2021. Obstacle height (I), obstacle spacing (II), drag coefficient as a sum of sea ice skin drag and form drag due to obstacles (III), total drag coefficient as a sum of the sea ice skin drag, form drag due to obstacles and floe edges and open water drag (IV).

Author contributions. All authors contributed in the development of the methods used, description of relevant information and the discussion and interpretation of the results. Alexander Mchedlishvili wrote most of the paper and the main algorithm for the analysis. Christof Lüpkes provided his expertise for the parts of the paper dealing with the parameterization used and the general mathematical background behind the study. Alek Petty was conferred with for all ICESat-2-related matters, contributed to the programming behind the analysis and helped structure the paper. Michel Tsamados contributed to the programming and acted as supervisor during a brief research stay at University College London when this paper was in the works. Gunnar Spreen acted as main supervisor and helped guide the development, analysis and writing stages of this study.

Competing interests. The authors declare that they have no conflict of interest.

Acknowledgements. This research was supported by the Deutsche Forschungsgemeinschaft (DFG, German Research Foundation) within the Transregional Collaborative Research Center TRR 172 "ArctiC Amplification: Climate Relevant Atmospheric and SurfaCe Processes, and Feedback Mechanisms (AC)[3]" (grant 268020496) and by European Union's Horizon 2020 research and innovation programme via project CRiceS (grant 101003826).

We thank NASA for providing ICESAt-2 and Operation IceBridge (OIB) data used in this study. We thank Marcus Huntemann, Robert Ricker, Marco Bagnardi, Giulia Castellani, Tom Johnson, Kyle Duncan and Sinead Farrell for their insightful discussion that helped in the preparation of this study.

References

Andreas, E. L., Horst, T. W., Grachev, A. A., Persson, P. O. G., Fairall, C. W., Guest, P. S., and Jordan, R. E.: Parametrizing turbulent exchange over summer sea ice and the marginal ice zone, Quarterly Journal of the Royal Meteorological Society, 136, 927–943, https://doi.org/10.1002/qj.618, 2010.

490 Arya, S. P. S.: Contribution of form drag on pressure ridges to the air stress on Arctic ice, Oceans and Atmospheres, 78(30), 7092–7099, https://doi.org/10.1029/JC078i030p07092, 1973.

Arya, S. P. S.: A drag partition theory for determining the large-scale roughness parameter and wind stress on the Arctic pack ice, Journal of Geophysical Research (1896-1977), 80, 3447–3454, https://doi.org/10.1029/JC080i024p03447, 1975.

Bagnardi, M., Kurtz, N. T., Petty, A. A., and Kwok, R.: Sea Surface Height Anomalies of the Arctic Ocean From ICESat-2: A First Exam-495 ination and Comparisons With CryoSat-2, Geophysical Research Letters, 48, e2021GL093 155, https://doi.org/10.1029/2021GL093155, 2021.

Birnbaum, G. and Lüpkes, C.: A new parameterization of surface drag in the marginal sea ice zone, Tellus A: Dynamic Meteorology and Oceanography, 54:1, 107–123, https://doi.org/10.3402/tellusa.v54i1.12121, 2002.

Bourke, R. H. and Garrett, R. P.: Sea ice thickness distribution in the Arctic Ocean, Cold Regions Science and Technology, 13, 259–280, 500 https://doi.org/10.1016/0165-232X(87)90007-3, 1987.

Castellani, G., Lüpkes, C., Hendricks, S., and Gerdes, R.: Variability of Arctic sea-ice topography and its impact on the atmospheric surface drag, J. Geophys. Res. Oceans, 119, 6743–6762, https://doi.org/10.1002/2013JC009712, 2014.

Duncan, K. and Farrell, S. L.: Determining Variability in Arctic Sea Ice Pressure Ridge Topography with ICESat-2, Geophysical Research Letters, n/a, e2022GL100 272, https://doi.org/10.1029/2022GL100272, 2022.

505 Elvidge, A. D., Renfrew, I. A., Brooks, I. M., Srivastava, P., Yelland, M. J., and Prytherch, J.: Surface Heat and Moisture Exchange in the Marginal Ice Zone: Observations and a New Parameterization Scheme for Weather and Climate Models, Journal of Geophysical Research: Atmospheres, 126, e2021JD034 827, https://doi.org/10.1029/2021JD034827, 2021.

Garbrecht, T., Lüpkes, C., Augstein, E., and Wamser, C.: Influence of a sea ice ridge on low-level airflow, Journal of Geophysical Research: Atmospheres, 104, 24 499–24 507, https://doi.org/10.1029/1999JD900488, 1999.

510 Garbrecht, T., Lüpkes, C., Hartmann, J., and Wolff, M.: Atmospheric drag coefficients over sea ice–validation of a parameterisation concept, Tellus A: Dynamic Meteorology and Oceanography, 54, 205–219, https://doi.org/10.3402/tellusa.v54i2.12129, 2002.

Gryanik, V. M. and Lüpkes, C.: An Efficient Non-iterative Bulk Parametrization of Surface Fluxes for Stable Atmospheric Conditions Over Polar Sea-Ice, Boundary-Layer Meteorology, 166, 301–325, https://doi.org/10.1007/s10546-017-0302-x, 2018.

Hanssen-Bauer, I. and Gjessing, Y. T.: Observations and model calculations of aerodynamic drag on sea ice in the Fram Strait, Tellus A, 40A, 515 151–161, https://doi.org/10.1111/j.1600-0870.1988.tb00413.x, 1988.

Hopkins, M. A.: Four stages of pressure ridging, Journal of Geophysical Research: Oceans, 103, 21 883–21 891, https://doi.org/10.1029/98JC01257, 1998.

Huber, P. J. and Ronchetti, E. M.: Regression, chap. 7, p. 172, John Wiley & Sons, Ltd, https://doi.org/10.1002/9780470434697.ch7, 2009.

Knowles, K. W.: A Mapping and Gridding Primer: Points, Pixels, Grids, and Cells, https://nsidc.org/data/user-resources/help-center/ 520 mapping-and-gridding-primer-points-pixels-grids-and-cells, 1993.

Kwok, R., Kacimi, S., Markus, T., Kurtz, N. T., Studinger, M., Sonntag, J. G., Manizade, S. S., Boisvert, L. N., , and Harbeck, J. P.: ICESat-2 Surface Height and Sea Ice Freeboard Assessed With ATM Lidar Acquisitions From Operation IceBridge, Geophysical Research Letters, 46, 11,228–11,236, https://doi.org/10.1029/2019GL084976, 2019a.

525   Kwok, R., Markus, T., Kurtz, N. T., Petty, A. A., Neumann, T. A., Farrell, S. L., Cunningham, G. F., Hancock, D. W., Ivanoff, A., and Wimert, J. T.: Surface Height and Sea Ice Freeboard of the Arctic Ocean From ICESat-2: Characteristics and Early Results, Journal of Geophysical Research: Oceans, 124, 6942–6959, https://doi.org/10.1029/2019JC015486, 2019b.

Kwok, R., Petty, A., Bagnardi, M., Wimert, J. T., Cunningham, G. F., Hancock, D. W., Ivanoff, A., and Kurtz, N.: ICESat-2 Algorithm Theoretical Basis Document for Sea Ice Products (ATL07/ATL10), Release 005, Algorithm theoretical basis document (atbd) for sea ice products, National Aeronautics and Space Administration, Goddard Space Flight Center, Greenbelt, Maryland 20771, https://nsidc.org/

530   sites/nsidc.org/files/technical-references/ICESat2_ATL07_ATL10_ATL20_ATL21_ATBD_r005.pdf, 2021a.

Kwok, R., Petty, A. A., Cunningham, G., Markus, T., Hancock, D., Ivanoff, A., Wimert, J., Bagnardi, M., Kurtz, N., and the ICESat-2 Science Team.: ATLAS/ICESat-2 L3A Sea Ice Height, Version 5, https://doi.org/10.5067/ATLAS/ATL07.005, 2021b.

Landy, J. C., Ehn, J. K., and Barber, D. G.: Albedo feedback enhanced by smoother Arctic sea ice, Geophysical Research Letters, 42, 10,714–10,720, https://doi.org/10.1002/2015GL066712, 2015.

535   Lüpkes, C. and Gryanik, V. M.: A stability-dependent parametrization of transfer coefficients for momentum and heat over polar sea ice to be used in climate models, Journal of Geophysical Research: Atmospheres, 120, 552–581, https://doi.org/10.1002/2014JD022418, 2015.

Lüpkes, C., Gryanik, V. M., Hartmann, J., and Andreas, E. L.: A parametrization, based on sea ice morphology, of the neutral atmospheric drag coefficients for weather prediction and climate models, Journal of Geophysical Research, 117, 205–219, https://doi.org/10.3402/tellusa.v54i2.12129, 2012.

540   Lüpkes, C., Gryanik, V. M., Rösel, A., Birnbaum, G., and Kaleschke, L.: Effect of sea ice morphology during Arctic summer on atmospheric drag coefficients used in climate models, Geophysical Research Letters, 40, 446–451, https://doi.org/10.1002/grl.50081, 2013.

MacGregor, J. A., Boisvert, L. N., Medley, B., Petty, A. A., Harbeck, J. P., Bell, R. E., Blair, J. B., Blanchard-Wrigglesworth, E., Buckley, E. M., Christoffersen, M. S., Cochran, J. R., Csathó, B. M., De Marco, E. L., Dominguez, R. T., Fahnestock, M. A., Farrell, S. L., Gogineni, S. P., Greenbaum, J. S., Hansen, C. M., Hofton, M. A., Holt, J. W., Jezek, K. C., Koenig, L. S., Kurtz, N. T., Kwok, R., Larsen,

545   C. F., Leuschen, C. J., Locke, C. D., Manizade, S. S., Martin, S., Neumann, T. A., Nowicki, S. M., Paden, J. D., Richter-Menge, J. A., Rignot, E. J., Rodríguez-Morales, F., Siegfried, M. R., Smith, B. E., Sonntag, J. G., Studinger, M., Tinto, K. J., Truffer, M., Wagner, T. P., Woods, J. E., Young, D. A., and Yungel, J. K.: The Scientific Legacy of NASA's Operation IceBridge, Reviews of Geophysics, 59, e2020RG000 712, https://doi.org/10.1029/2020RG000712, 2021.

Magruder, L. A., Brunt, K. M., and Alonzo, M.: Early ICESat-2 on-orbit Geolocation Validation Using Ground-Based Corner Cube Retro-

550   Reflectors, Remote Sensing, 12, https://doi.org/10.3390/rs12213653, 2020.

Magruder, L. A., Brunt, K. M., Neumann, T., Klotz, B., and Alonzo, M.: Passive Ground-Based Optical Techniques for Monitoring the On-Orbit ICESat-2 Altimeter Geolocation and Footprint Diameter, Earth and Space Science, 8, e2020EA001 414, https://doi.org/10.1029/2020EA001414, 2021.

Martin, C. F., Krabill, W. B., Manizade, S. S., Russell, R. L., Sonntag, J. G., Swift, R. N., and Yungel, J. K.: Airborne Topographic Map-

555   per Calibration Procedures and Accuracy Assessment, Tech. Rep. Technical Memorandum, 215891., National Aeronautics and Space Administration, Greenbelt, Maryland 20771. Goddard Space Flight Center., https://ntrs.nasa.gov/api/citations/20120008479/downloads/20120008479.pdf, 2012.

Martin, T., Tsamados, M., Schroeder, D., and Feltham, D. L.: The impact of variable sea ice roughness on changes in Arctic Ocean surface stress: A model study, J. Geophys. Res. Oceans, 121(3), 1931–1952, https://doi.org/10.1002/2015JC011186, 2016.

560 Mchedlishvili, A., Spreen, G., Lüpkes, C., Tsamados, M., and Petty, A.: Gridded pan-Arctic total neutral atmospheric 10-m drag coefficient estimates derived from ICESat-2 ATL07 sea ice height data, https://doi.org/10.1594/PANGAEA.951333, 2022.

Melsheimer, C. and Spreen, G.: AMSR2 ASI sea ice concentration data, Arctic, version 5.4 (NetCDF) (July 2012 - December 2019), https://doi.org/10.1594/PANGAEA.898399, 2019.

Melsheimer, C., Spreen, G., Ye, Y., and Shokr, M.: Antarctic sea ice types from active and passive microwave remote sensing, The Cryosphere
565 Discussions, 2022, 1–23, https://doi.org/10.5194/tc-2021-381, 2022.

Mock, S. J., Hartwell, A. D., and Hibler, W. D.: Spatial aspects of pressure ridge statistics, Journal of Geophysical Research (1896-1977), 77, 5945–5953, https://doi.org/10.1029/JC077i030p05945, 1972.

Neumann, T. A., Martino, A. J., Markus, T., Bae, S., Bock, M. R., Brenner, A. C., Brunt, K. M., Cavanaugh, J., Fernandes, S. T., Hancock, D. W., Harbeck, K., Lee, J., Kurtz, N. T., Luers, P. J., Luthcke, S. B., Magruder, L., Pennington, T. A., Ramos-Izquierdo,
570 L., Rebold, T., Skoog, J., and Thomas, T. C.: The Ice, Cloud, and Land Elevation Satellite – 2 mission: A global geolocated photon product derived from the Advanced Topographic Laser Altimeter System, Remote Sensing of Environment, 233, 111 325, https://doi.org/10.1016/j.rse.2019.111325, 2019.

Petty, A. A., Tsamados, M. C., Kurtz, N. T., Farrell, S. L., Newman, T., Harbeck, J. P., Feltham, D. L., and Richter-Menge, J. A.: Characterizing Arctic sea ice topography using high-resolution IceBridge data, The Cryosphere, 10, 1161–1179, https://doi.org/10.5194/tc-10-
575 1161-2016, 2016.

Petty, A. A., Tsamados, M. C., and Kurtz, N. T.: Atmospheric form drag coefficients over Arctic sea ice using remotely sensed ice topography data, spring 2009–2015, J. Geophys. Res. Surf., 122, 1472–1490, https://doi.org/10.1002/2017JF004209, 2017.

Ricker, R., Fons, S., Jutila, A., Hutter, N., Duncan, K., Farrell, S. L., Kurtz, N. T., and Hansen, R. M. F.: Linking scales of sea ice surface topography: evaluation of ICESat-2 measurements with coincident helicopter laser scanning during MOSAiC, EGUsphere, 2022, 1–27,
580 https://doi.org/10.5194/egusphere-2022-1122, 2022.

Serreze, M. C. and Barry, R. G.: Processes and impacts of Arctic amplification: A research synthesis, Global and Planetary Change, 77, 85–96, https://doi.org/10.1016/j.gloplacha.2011.03.004, 2011.

Shokr, M., Lambe, A., and Agnew, T.: A New Algorithm (ECICE) to Estimate Ice Concentration From Remote Sensing Observations: An Application to 85-GHz Passive Microwave Data, IEEE Transactions on Geoscience and Remote Sensing, 46, 4104–4121,
585 https://doi.org/110.1109/TGRS.2008.2000624, 2008.

Spreen, G., Kaleschke, L., and Heygster, G.: Sea ice remote sensing using AMSR-E 89-GHz channels, Journal of Geophysical Research: Oceans, 113, https://doi.org/10.1029/2005JC003384, 2008.

Steele, M., Zhang, J., Rothrock, D., and Stern, H.: The force balance of sea ice in a numerical model of the Arctic Ocean, J. Geophys. Res. Oceans, 102(C9), 21 061–21 079, https://doi.org/10.1029/97JC01454, 1997.

590 Steiner, N., Harder, M., and Lemke, P.: Sea-ice roughness and drag coefficients in a dynamic–thermodynamic sea-ice model for the Arctic, Tellus A: Dynamic Meteorology and Oceanography, 51:5, 964–978, https://doi.org/10.3402/tellusa.v51i5.14505, 1999.

Stroeve, J., Serreze, M., Holland, M., Kay, J., Malanik, J., and Barrett, A.: Atmospheric drag coefficients over sea ice–validation of a parameterisation concept, Climatic Change, 110, 1005–1027, https://doi.org/10.1007/s10584-011-0101-1, 2012.

Studinger, M.: IceBridge ATM L1B Elevation and Return Strength, Version 2, https://doi.org/10.5067/19SIM5TXKPGT, 2013.

595 Studinger, M.: IceBridge ATM L1B Elevation and Return Strength, Version 2, Tech. rep., National Aeronautics and Space
Administration, Boulder, Colorado USA. NASA National Snow and Ice Data Center Distributed Active Archive Center.,
https://doi.org/10.5067/19SIM5TXKPGT., M. 2013, updated 2020.

Studinger, M., Manizade, S. S., Linkswiler, M. A., and Yungel, J. K.: High-resolution imaging of supraglacial hydrological features
on the Greenland Ice Sheet with NASA's Airborne Topographic Mapper (ATM) instrument suite, The Cryosphere, 16, 3649–3668,
600 https://doi.org/10.5194/tc-16-3649-2022, 2022.

Thorndike, A. S. and Colony, R.: Sea ice motion in response to geostrophic winds, J. Geophys. Res. Oceans, 87(C8), 5845–5852,
https://doi.org/10.1029/JC087iC08p05845, 1982.

Thorndike, A. S., Rothrock, D. A., Maykut, G. A., and Colony, R.: The thickness distribution of sea ice, Journal of Geophysical Research
(1896-1977), 80, 4501–4513, https://doi.org/10.1029/JC080i033p04501, 1975.

605 Tilling, R., Kurtz, N. T., Bagnardi, M., Petty, A. A., and Kwok, R.: Detection of Melt Ponds on Arctic Summer Sea Ice From ICESat-2,
Geophysical Research Letters, 47, e2020GL090 644, https://doi.org/10.1029/2020GL090644, 2020.

Timco, G. and Burden, R.: An analysis of the shapes of sea ice ridges, Cold Regions Science and Technology, 25, 65–77,
https://doi.org/10.1016/S0165-232X(96)00017-1, 1997.

Tremblay, L.-B. and Mysak, L. A.: Modeling Sea Ice as a Granular Material, Including the Dilatancy Effect, J. Phys. Oceanogr, 27(11),
610 2342–2360, https://doi.org/10.1175/1520-0485(1997)027<2342:MSIAAG>2.0.CO;2, 1977.

Tsamados, M., Feltham, D. L., Schroeder, D., Flocco, D., Farrell, S. L., Kurtz, N., Laxon, S. W., , and Bacon, S.: Impact of Vari-
able Atmospheric and Oceanic Form Drag on Simulations of Arctic Sea Ice, Journal of Physical Oceanography, 44(5), 1329–1353,
https://doi.org/10.1175/JPO-D-13-0215.1, 2014.

Tsamados, M., Feltham, D., A. Petty, D., Schroeder, and Flocco, D.: Processes controlling surface, bottom and lateral melt of Arctic sea ice
615 in a state of the art sea ice model, Phil. Trans. R. Soc. A, 373, https://doi.org/10.1098/rsta.2014.0167, 2016.

Ye, Y., Heygster, G., and Shokr, M.: Improving Multiyear Ice Concentration Estimates With Reanalysis Air Temperatures, IEEE Transactions
on Geoscience and Remote Sensing, 54, 2602–2614, https://doi.org/10.1109/TGRS.2015.2503884, 2016a.

Ye, Y., Shokr, M., Heygster, G., and Spreen, G.: Improving Multiyear Sea Ice Concentration Estimates with Sea Ice Drift, Remote Sensing,
8, https://doi.org/10.3390/rs8050397, 2016b.

620 Yu, X., Rinke, A., Dorn, W., Spreen, G., Lüpkes, C., Sumata, H., and Gryanik, V. M.: Evaluation of Arctic sea ice drift and its dependency
on near-surface wind and sea ice conditions in the coupled regional climate model HIRHAM–NAOSIM, The Cryosphere, 14, 1727–1746,
https://doi.org/10.5194/tc-14-1727-2020, 2020.